



Alignment of semiconducting graphene nanoribbons on vicinal Ge(001)

Journal:	<i>Nanoscale</i>
Manuscript ID	NR-ART-01-2019-000713.R1
Article Type:	Paper
Date Submitted by the Author:	20-Feb-2019
Complete List of Authors:	Jacobberger, Robert; University of Wisconsin-Madison, Murray, Ellen; University of Wisconsin-Madison Fortin-deschenes, Matthieu; Polytechnique Montreal, Göttl, Florian; University of Wisconsin Madison, Chemical Engineering Behn, Wyatt; University of Wisconsin-Madison Krebs, Zachary; University of Wisconsin-Madison Levesque, Pierre; Universite de Montreal Savage, Don; University of Wisconsin-Madison, Material Science and Engineering and Physics Smoot, Charles; University of Wisconsin-Madison Lagally, Max; Univeristy of Wisconsin-Madison, Materials Science and Engineering Desjardins, Patrick; Polytechnique Montreal Martel, Richard; Université de Montréal, Chemistry Brar, Victor; University of Wisconsin Madison Graduate School, Physics Moutanabbir, Oussama; Ecole Polytechnque de Montreal, Engineering Physics Mavrikakis, Manos ; University fo Wisconsin - Madison, Arnold , Michael; University of Wisconsin Madison, Chemical Engineering



Alignment of semiconducting graphene nanoribbons on vicinal Ge(001)

Received 00th January 20xx,
Accepted 00th January 20xx

DOI: 10.1039/x0xx00000x

www.rsc.org/

Robert M. Jacobberger,^a Ellen A. Murray,^b Matthieu Fortin-Deschênes,^c Florian Göttl,^b Wyatt A. Behn,^d Zachary J. Krebs,^d Pierre L. Levesque,^e Donald E. Savage,^a Charles Smoot,^a Max G. Lagally,^a Patrick Desjardins,^c Richard Martel,^e Victor Brar,^d Oussama Moutanabbir,^c Manos Mavrikakis,^b Michael S. Arnold^{a*}

Chemical vapor deposition of CH₄ on Ge(001) can enable anisotropic growth of narrow, semiconducting graphene nanoribbons with predominately smooth armchair edges and high-performance charge transport properties. However, such nanoribbons are not aligned in one direction but instead grow perpendicularly, which is not optimal for integration into high-performance electronics. Here, it is demonstrated that vicinal Ge(001) substrates can be used to synthesize armchair nanoribbons, of which ~90% are aligned within $\pm 1.5^\circ$ perpendicular to the miscut. When the growth rate is slow, graphene crystals evolve as nanoribbons. However, as the growth rate increases, the uphill and downhill crystal edges evolve asymmetrically. This asymmetry is consistent with stronger binding between the downhill edge and the Ge surface, for example due to different edge termination as shown by density functional theory calculations. By tailoring growth rate and time, nanoribbons with sub-10 nm widths that exhibit excellent charge transport characteristics, including simultaneous high on-state conductance of 8.0 μS and high on/off conductance ratio of 570 in field-effect transistors, are achieved. Large-area alignment of semiconducting ribbons with promising charge transport properties is an important step towards understanding the anisotropic nanoribbon growth and integrating these materials into scalable, future semiconductor technologies

1. Introduction

Graphene nanoribbons are promising candidates for semiconductor electronics because, unlike continuous graphene sheets, they can have bandgaps suitable for substantial conductance modulation at room temperature. The bandgap depends on ribbon width and edge structure, and the largest bandgaps are expected in ribbons < 10 nm wide with smooth armchair edges (*i.e.*, C–C bonds parallel to the ribbon long-axis).¹ Semiconducting nanoribbons also have potential to achieve high charge carrier mobility² and velocity,³ current density,⁴ and electrical³ and thermal⁵ conductivity, and their atomic thickness enables excellent electrostatic control.⁶ To improve feasibility of nanoribbon integration into semiconductor electronics and maximize device performance, ribbons must be highly aligned in one direction. For example, in field-effect transistors (FETs), unaligned ribbons can result in charge screening and lengthen the

charge conduction pathway, decreasing on-state conductance and on/off conductance ratio.^{7,8}

One of the most successful approaches to fabricate aligned nanoribbons while also achieving high precision over ribbon width and edge structure is polymerization and cyclodehydrogenation of molecular precursors on stepped Au(788) surfaces.^{9–13} This technique yields densely-packed, aligned ribbons with sub-2 nm widths and atomically-smooth armchair edges, in which the average distance between the long-axis of neighboring ribbons is 1–2 nm¹⁴ and ribbons are aligned within $\sim 9^\circ$.¹² However, these ribbons are typically only 20–30 nm in length,^{9,10,13,14} making them difficult to electrically contact and integrate into scalable technologies. The ribbons also have relatively large bandgaps due to their especially narrow widths, leading to Schottky barriers at the ribbon/electrode interface and, consequently, formation of high-impedance electrical contacts.^{15–17} Furthermore, the high ribbon density can lead to electrostatic screening and, thus, reduced conductance modulation in FETs.^{7,8}

Replicating the precise control over ribbon alignment, width, and edge structure afforded by polymerization/cyclodehydrogenation while also achieving sub-10 nm ribbons that are wider (to obtain smaller bandgaps) and longer (to facilitate widespread integration) has been difficult. Aligned ribbons can be fabricated using subtractive lithography of continuous graphene.^{18,19} However, the ribbons have rough, defective edges that degrade the exceptional transport properties expected in pristine ribbons, and ribbons with sub-10 nm widths cannot be fabricated to induce technologically relevant bandgaps $\gg k_B T$ at room temperature.

^a Department of Materials Science and Engineering, University of Wisconsin-Madison, Madison, Wisconsin 53706, United States.

^b Department of Chemical and Biological Engineering, University of Wisconsin-Madison, Madison, Wisconsin 53706, United States.

^c Department of Engineering Physics, Polytechnique Montréal, Montréal, Québec H3C 2A7, Canada

^d Department of Physics, University of Wisconsin-Madison, Madison, Wisconsin 53706, United States.

^e Department of Chemistry, Université de Montréal, Montréal, Québec H3C 3J7, Canada

Electronic Supplementary Information (ESI) available. See DOI: 10.1039/x0xx00000x

Nanoribbon alignment has also been achieved via growth on SiC nanofacets²⁰ and Ni nanobars,²¹ substrate-controlled, metal-assisted etching of continuous graphene,²² and unzipping carbon nanotubes.²³ Semiconducting ribbons, however, have not been reported via growth on SiC nanofacets and Ni nanobars. Metal-assisted etching and growth on nanobars suffer from poor yield, inability to controllably produce ribbons with sub-10 nm widths, and formation of ribbons with relatively rough edges. Fabricating aligned ribbons with controlled edges via nanotube unzipping relies on the requisite ability to align nanotubes from solution, which is a major challenge by itself.^{24, 25}

Alternately, we recently reported a scalable, bottom-up technique to directly synthesize narrow, polydisperse nanoribbons with predominately smooth armchair edges via chemical vapor deposition (CVD).²⁶ In this process, CVD of CH₄ on Ge(001) at ~910 °C in a flow of H₂ and Ar results in anisotropic growth of ribbons, provided the growth rate is relatively slow (nanometers per hour). In this regime, ribbons with sub-10 nm width can still have lengths of hundreds of nanometers. The ribbons grow with self-defining armchair edges, and width can be continuously tuned to nearly zero by controlling growth rate and time. For example, scanning tunneling microscopy (STM) has shown the ribbon edges consist of smooth armchair segments, with edge roughness of < 5 Å over lengths of tens of nanometers, and has confirmed synthesis of ribbons as narrow as 2 nm.^{26, 27} In FETs, these ribbons have simultaneously exhibited on/off conductance ratio of 2×10⁴ and on-state conductance of 5 μS, among the highest charge transport metrics reported for ribbons.²⁸ Width polydispersity leads to variability in FET on/off conductance ratio, although initiating nanoribbon synthesis from seeds provides a promising path to overcome this polydispersity.²⁹ Furthermore, such ribbon synthesis has only been demonstrated on Ge(001) surfaces.

Nanoribbons that spontaneously nucleate and grow on Ge(001) also adopt two predominate orientations roughly aligned along the perpendicular Ge<110> directions with equal probability, limiting ribbon alignment and packing density.²⁶ We have recently shown unidirectional alignment can be realized by initiating growth from nanoscale graphene seeds with rationally-controlled lattice orientation.²⁹ The lattice orientation of the ribbon matches that of the seeds from which they grow, the ribbons always have armchair edges, and growth anisotropy is maximized when the armchair direction is along Ge<110>. Thus, by controlling the seed armchair direction to be along Ge[110] or Ge[$\bar{1}10$], the long-axis of each of the resulting armchair ribbons also aligns unidirectionally along Ge [110] or Ge[$\bar{1}10$], respectively.

These data suggest that if graphene nuclei that naturally form can be globally aligned, it may be possible to orient ribbons unidirectionally without seeding. Such alignment is possible via epitaxial growth on Ge(110) and is a result of strong binding between graphene and Ge step edges.^{30, 31} However, anisotropic growth cannot be driven on Ge(110) to yield ribbons.²⁶ If steps on Ge(001) can be engineered in one direction, for example by introducing a miscut, it may be possible to realize epitaxial alignment and, consequently, aligned ribbons without seeds, which is desirable for improved manufacturability and furthering the fundamental understanding of anisotropic ribbon synthesis.

Here, we find by conducting growth on vicinal Ge surfaces, ~90% of the crystals can evolve as armchair nanoribbons oriented

perpendicular to the miscut. When the growth rate is slow, graphene crystals evolve as nanoribbons. However, as growth rate increases, graphene islands transition from being rectangular to trapezoidal to semicircular. Density functional theory (DFT) calculations indicate this asymmetric evolution may be due to different chemical binding or termination at the downhill and uphill ribbon edges. We also demonstrate the growth conditions can be tailored to directly synthesize aligned semiconducting nanoribbons with sub-10 nm widths, and these ribbons can exhibit promising charge transport properties such as high on/off conductance ratio and on-state conductance.

2. Results and discussion

2.1. Effect of miscut on nanoribbon growth

First, we explore graphene synthesis on Ge(001) surfaces with 0°, 6°, and 9° miscut towards Ge[110] (*i.e.*, Ge(001)-0°, -6°, and -9°, respectively) to determine the effect of miscut on ribbon growth and crystallinity and the effect of growth rate on crystal shape evolution and anisotropy. Relatively wide ribbons (~10–100 nm in width) are synthesized to ease in characterization of crystal dimensions and shapes using scanning electron microscopy (SEM). Later, we synthesize narrower ribbons with sub-10 nm widths, simply by decreasing the growth rate or time, enabling characterization of charge transport properties of semiconducting nanoribbons in FETs.

Fig. 1d-f shows SEM images of isolated graphene islands grown on each surface. To determine the effect of miscut on synthesis, crystal alignment, width, length, and aspect ratio are characterized with SEM (Fig. 1g-j and Fig. S1). On Ge(001)-0°, graphene crystals evolve as high-aspect ratio nanoribbons with their long-axis rotated +2.8° or -2.8° from Ge<110>,²⁶ resulting in four ribbon orientations roughly aligned along perpendicular Ge[110] and Ge[$\bar{1}10$] directions with equal probability. Ribbons oriented near Ge[110] and Ge[$\bar{1}10$] have similar widths, lengths, and aspect ratios (Fig. 1h-j), which is expected because these directions are equivalent on Ge(001)-0°.

In contrast, as the miscut angle increases, the long-axis of the crystals becomes preferentially oriented perpendicular to the miscut, resulting in unidirectional alignment of a majority of the crystals. For example, 73% and 91% of the crystals on Ge(001)-6° and Ge(001)-9°, respectively, are perpendicular to the miscut (Fig. 1g). Moreover, the more prevalent crystals aligned perpendicular to the miscut are narrower and have higher aspect ratios (*i.e.* they can be ribbons, with longer lengths per width) than the less common crystals parallel to the miscut (Fig. 1h-j), which evolve as more isotropic quadrilaterals. These trends are depicted schematically in Fig. 1a-c. Crystals perpendicular to the miscut can also be much wider than the average Ge terrace width of ~1 nm, and thus are not confined to a single terrace but instead can grow across Ge steps. The probability of graphene growth uphill and downhill, however, is not equivalent, as demonstrated below. Furthermore, the ribbon length does not saturate and is similar on each surface, indicating either that the length is not limited by kinks in Ge steps or that kinks rearrange to form straight Ge steps during growth.

X-ray diffraction (XRD) shows the miscut in these Ge(001)-6° and Ge(001)-9° wafers deviates azimuthally from Ge[110] by $4 \pm 1^\circ$ and $0.5 \pm 1^\circ$, respectively. Thus, we cannot conclude whether the higher alignment on Ge(001)-9° is due to larger miscut angle or smaller miscut deviation azimuthally from Ge[110]. Nonetheless, ~90% of nanoribbons can be aligned unidirectionally on miscut surfaces. It is possible alignment can be further increased, for example by growing on surfaces with a larger miscut angle or less azimuthal deviation in

the miscut from Ge[110]. Ribbon alignment also depends on anneal time and H₂:CH₄ flux ratio used during synthesis (Fig. S2). In the following studies, we primarily focus on characterization of the more common anisotropic nanoribbons perpendicular to the miscut, rather than the crystals parallel to the miscut with lower aspect ratios.

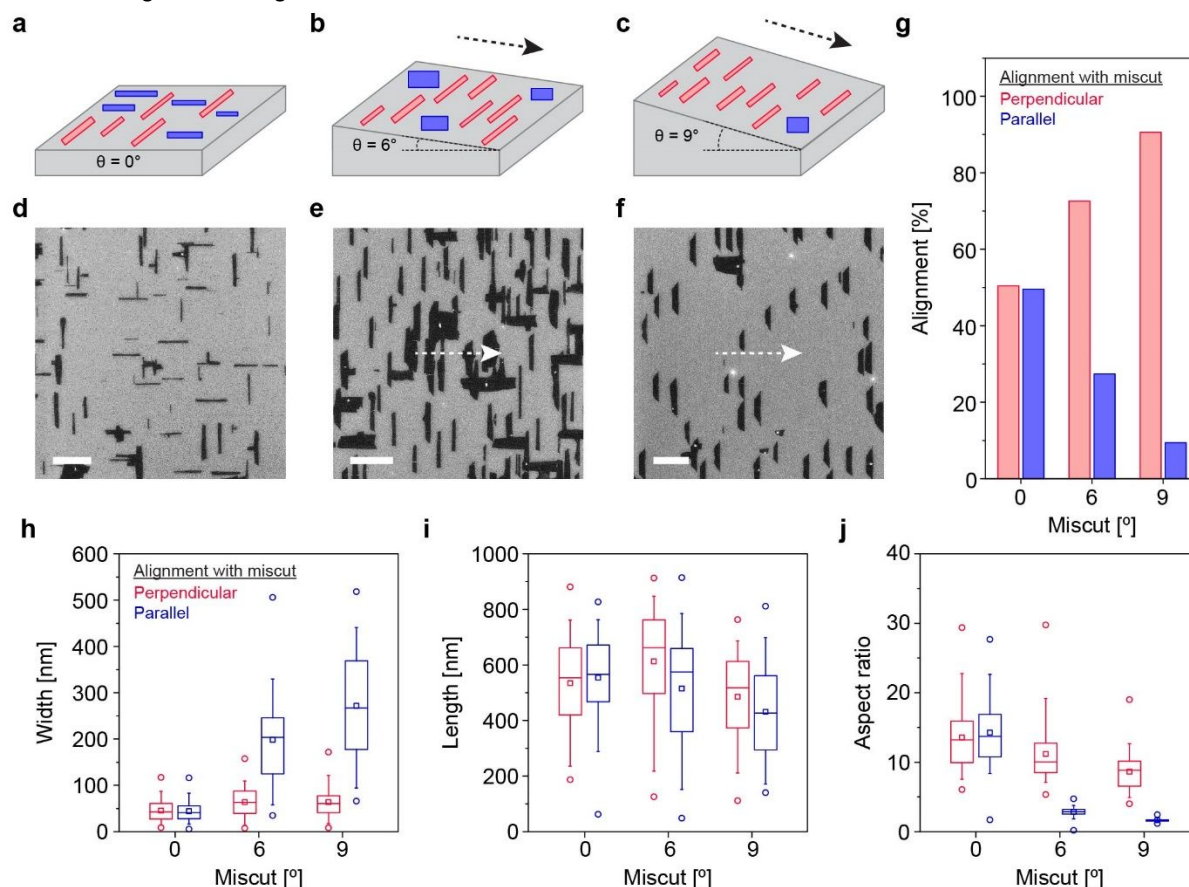


Fig. 1. Effect of Ge miscut on nanoribbon growth. (a-f) Schematic diagrams (a-c) and SEM images (d-f) of graphene crystals grown on Ge(001) with 0° (a,d), 6° (b,e), and 9° (c,f) miscut toward Ge[110]. Red and blue crystals in a-c are perpendicular and parallel, respectively, to the miscut. Dashed arrows in b,c,e,f point downhill. Scale bars in d-f are 1 μm . (g-j) Alignment (g), width (h), length (i), and aspect ratio (j) versus miscut angle for ribbons oriented perpendicular (red, left) and parallel (blue, right) to the miscut on Ge(001)-6° and Ge(001)-9° and oriented along [110] and $\bar{1}\bar{1}0$ on Ge(001)-0°. Horizontal lines in the boxes in h-j define 25th, 50th, and 75th percentiles, whiskers indicate 5th and 95th percentiles, circles define the range, and squares give the mean.

2.2. Dependence of ribbon anisotropy and crystal shape evolution on growth rate

For specific growth conditions, nanoribbons grown perpendicular to the miscut on Ge(001)-6° and Ge(001)-9° are wider and less anisotropic than those directed along $\langle 110 \rangle$ on Ge(001)-0° (Fig. 1h-j). However, it has been found that the anisotropy on Ge(001)-0° can be increased by reducing the growth rate, either by increasing H₂ flux or decreasing CH₄ flux.²⁶ The H₂ and CH₄ fluxes are also important factors for controlling the shape evolution³²⁻³⁴ and crystallinity³⁵⁻³⁷ of graphene grown on metal surfaces.

Therefore, we next study the effect of H₂:CH₄ flux ratio, and thus growth rate, on graphene island morphology and crystal shape evolution. Graphene is synthesized using progressively larger growth

rates by reducing the H₂:CH₄ ratio from 50 to 22 to 16, and crystal shapes are characterized with SEM (Fig. 2a-i). Raman spectroscopy (Fig. S3) shows that graphene crystals have relatively low defect density when H₂:CH₄ is at least 22, as the D band is immeasurably small with a D:G peak amplitude ratio < 0.1 . When H₂:CH₄ is 16, defect density is increased compared to graphene grown using higher H₂:CH₄, as indicated by the measurable presence of the D band and D:G peak amplitude ratio ~ 0.25 .

Fig. S4 and S5 show for each vicinal surface, the crystal shape anisotropy decreases with increasing growth rate. Furthermore, for a given rate, anisotropy is largest on Ge(001)-0° and smallest on Ge(001)-9°. For example, on Ge(001)-0°, aspect ratio decreases from 35.5 ± 9.8 to 9.7 ± 4.0 as growth rate increases from 18.1 ± 4.6 to $270 \pm 130 \text{ nm h}^{-1}$, respectively, whereas on Ge(001)-9°, aspect ratio

decreases from 12.6 ± 4.0 to 3.32 ± 0.39 as growth rate increases from 30.1 ± 6.9 to 480 ± 200 nm h⁻¹, respectively.

Growth rate also affects shape evolution of graphene crystals. When growth rate is slow (*i.e.*, large H₂:CH₄), crystals evolve as high-aspect ratio nanoribbons in which both edges along the long-axis are approximately the same length (Fig. 2a,d,g). As growth rate increases (*i.e.*, H₂:CH₄ decreases) on Ge(001)-0°, both edges continue to be nearly the same length, although some edges become less straight and roughen (Fig. 2b,c). In contrast, on Ge(001)-6° and Ge(001)-9°, the downhill crystal edge becomes longer than the uphill edge, forming trapezoids (Fig. 2e,h). As growth rate increases further, the uphill edge becomes rough and rounded, forming hemisphere-like shapes (Fig. 2f,i). Interestingly, the downhill edge stays relatively

smooth and straight for hundreds of nanometers, indicating the uphill and downhill edges are inequivalent growth fronts, as studied further below.

Notably, this crystal shape transition is primarily a result of increasing growth rate, and either has no dependence or much weaker dependence on crystal size. For example, crystals as narrow as ~15 nm can grow as trapezoids at a growth rate of ~240 nm h⁻¹ (Fig. 2e,h), but crystals as wide as ~50 nm can evolve as rectangles at a slower growth rate of ~30 nm h⁻¹ (Fig. 2d,g). Similarly, crystals as narrow as ~15 nm can grow as semicircles at a growth rate of ~470 nm h⁻¹ (Fig. 2f,i), but crystals as wide as ~200 nm can evolve as trapezoids at a slower growth rate of ~240 nm h⁻¹ (Fig. 2e,h).

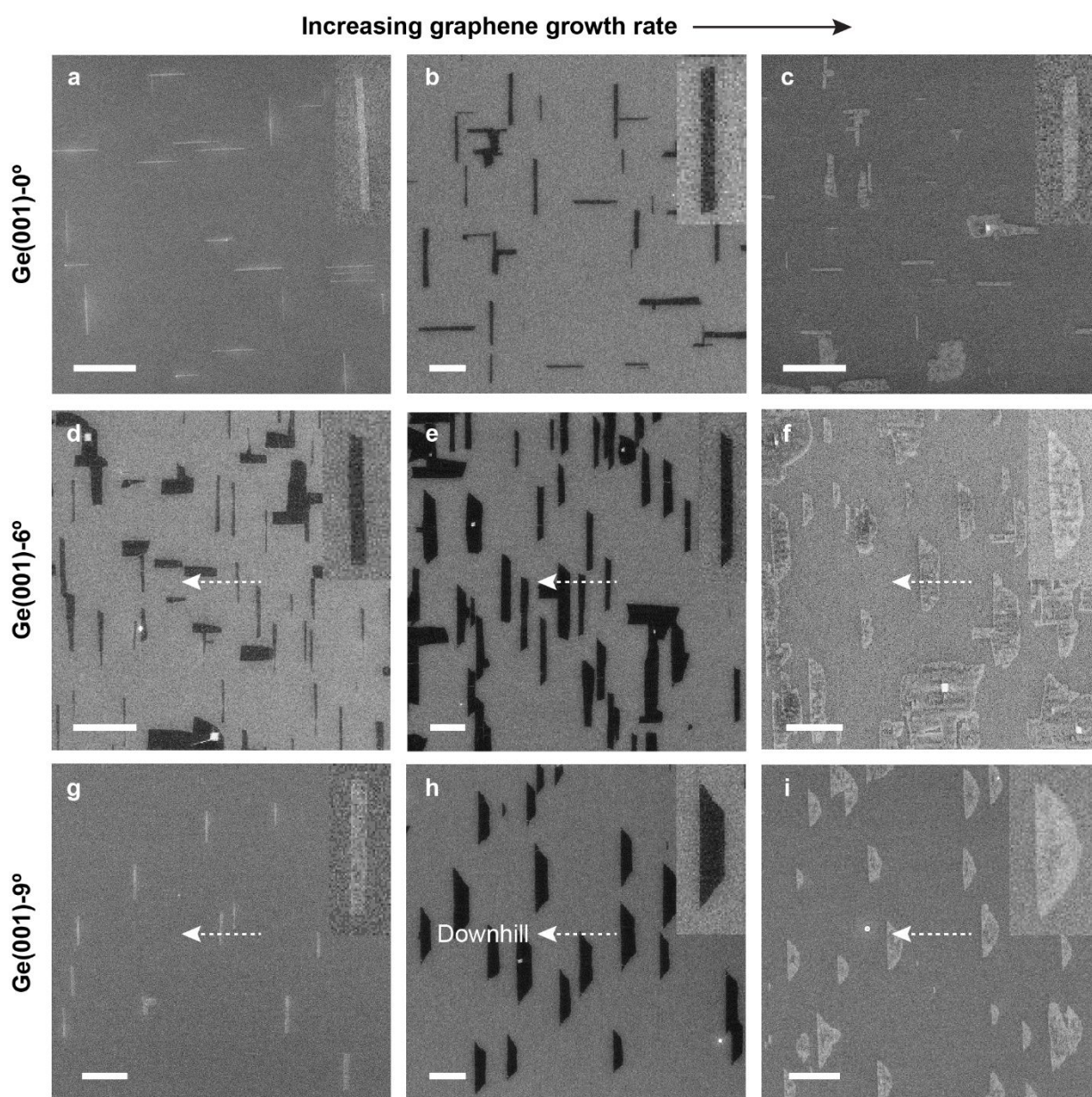


Fig. 2. Effect of growth rate on crystal shape evolution and anisotropy. (a-i) SEM images of graphene crystals grown on Ge(001)-0° (a-c), Ge(001)-6° (d-f), and Ge(001)-9° (g-i) with increasing growth rate. Dashed arrows point downhill, as determined by XRD. Scale bars are 500 nm. Insets are magnified images of a representative crystal. Contrast reversal is attributed to amorphous carbon deposition upon sample exposure to the electron beam and oxidation of the Ge surface (Fig. S7 and S8).

Nanoscale

ARTICLE

2.3. Electron microscopy and diffraction studies

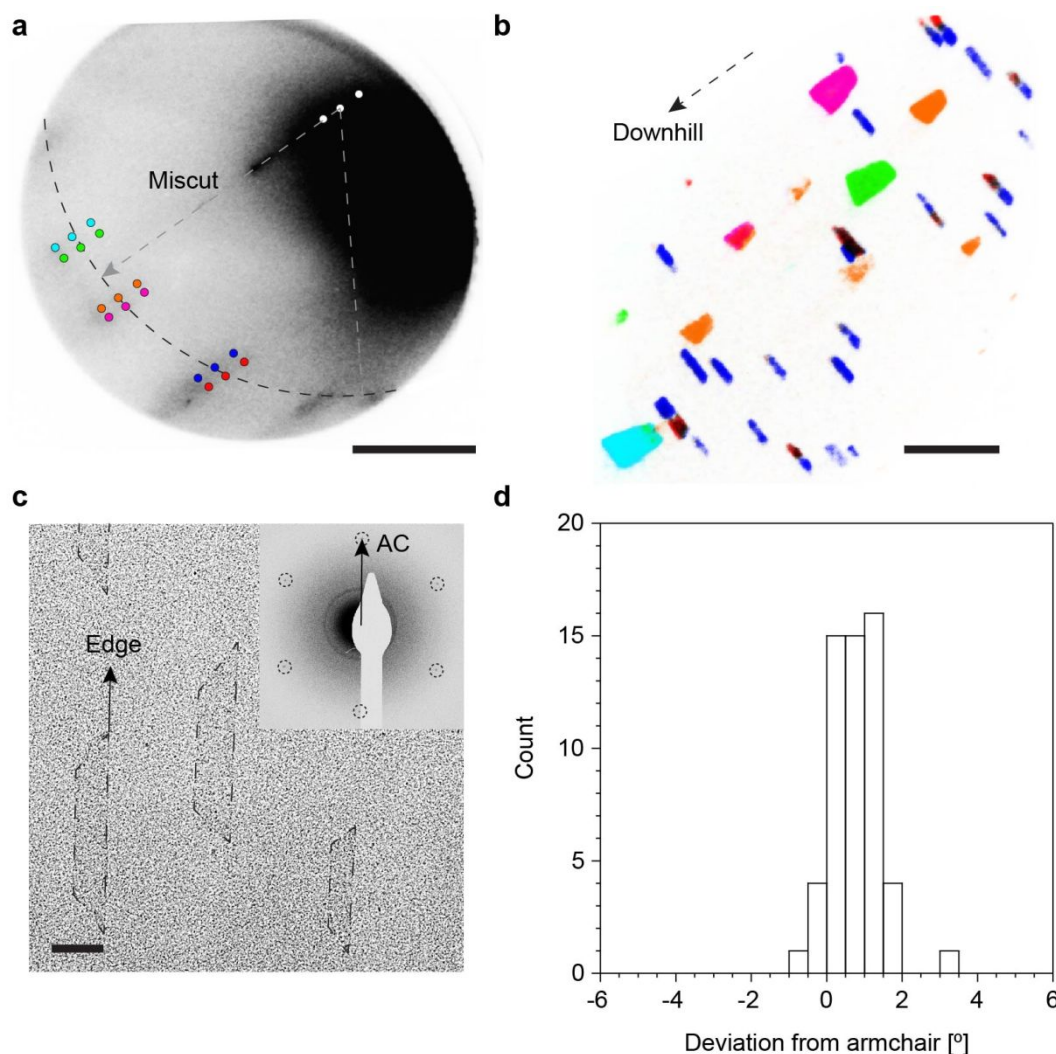
Low-energy electron microscopy (LEEM) and diffraction (LEED) are used to characterize the graphene crystallographic orientation with respect to the Ge(001)-9° surface. Fig. 3a shows a LEED pattern from isolated crystals on Ge(001)-9° (Fig. S9), in which gray dashed lines enclose a circular sector of the pattern with central angle of 60°. Splitting of the (00) LEED spot is observed, characteristic of vicinal surfaces.³⁸ This splitting is also observed for graphene {01} spots. In Fig. 3a, the three (00) spots are highlighted in white, and the set of graphene diffraction spots corresponding to the central (00) spot follow the dashed arc.

There are six main graphene orientations on Ge(001)-9°, as highlighted in cyan, green, orange, magenta, blue, and red in Fig. 3a in which the armchair graphene direction is rotated from the miscut direction by -8.5, -7.0, 5.8, 8.2, 28.5, and 31.2°, respectively. Dark-field LEEM is conducted to correlate each set of diffraction patterns with the island morphology and alignment. Fig. 3b shows a composite image of graphene crystals with each of the six diffraction patterns. These data show the diffraction spots in red and blue correspond to high-aspect ratio ribbons oriented perpendicular to

the miscut, indicating the ribbon edges are roughly aligned along the armchair direction. Some islands are single-crystals, whereas others are bi-crystals in which approximately half the ribbon has an orientation rotated $\sim 2.7^\circ$ from that in the other half. Single- and bi-crystals were also observed on Ge(001)-0°. Existence of bi-crystals indicates ribbons nucleate in their center and then grow in opposite directions along their length. Interestingly, crystals with low-aspect ratios (*i.e.*, cyan, green, orange, and magenta data in Fig. 3a,b) have rotated lattices with respect to that of ribbons, indicating anisotropic ribbon growth is only driven when there is a specific relative orientation between graphene and the underlying Ge surface, similar to growth on Ge(001)-0°. ^{26, 29}

Transmission electron microscopy (TEM) and selected-area electron diffraction (SAED) are used to more precisely characterize crystallographic alignment of ribbon edges grown on Ge(001)-9°. Fig. 3c provides an SAED pattern from the labelled crystal, showing the smooth crystal edge is aligned closely to the armchair direction. Analysis of 56 crystals indicates the edges are aligned, on average, within 0.85° of the armchair direction (Fig. 3d), similar to the deviation of 1.6° for ribbons grown on Ge(001)-0°. ²⁹

Fig. 3. LEEM and TEM characterization of graphene grown on Ge(001)-9°. (a) LEED pattern in which the {01} graphene diffraction spots are highlighted in cyan, green, orange, magenta, blue, and red. {00} diffraction spots are highlighted in white. (b) Superposition of dark-field



images in which the color of each crystal corresponds to the {01} spot with the same color in a. Dashed arrow points downhill, as determined from the trapezoidal island orientation. Scale bar is 2 μm . (c) TEM image of graphene crystals with their edges highlighted by dashed lines. Inset is an SAED pattern from the labelled crystal. The armchair (AC) direction and ribbon long-axis are aligned. Scale bar is 200 nm. (d) Histogram of edge deviation from the armchair direction for 56 ribbons, as determined from TEM and SAED.

2.4. Growth of nanoribbons with sub-10 nm widths

Most ribbons in Fig. 1, 2, and 3 are relatively wide (~ 10 – 100 nm in width). However, narrower nanoribbons can also be synthesized by decreasing growth rate or time. For example, Fig. 4a,b shows aligned ribbons with average width of 12.2 ± 3.6 nm can be grown using short growth time of 2.5 h at ~ 30 nm h^{-1} . Even narrower

nanoribbons with width of 3–4 nm (below the SEM resolution of ~ 10 nm) are grown by further decreasing growth time to 40 min and rate to ~ 10 nm h^{-1} , as shown in Fig. 4c,d. The ribbon edges are relatively smooth, as width varies < 5 Å over $> 90\%$ of the ribbon length in 4d. Charge transport of ribbons with sub-10 nm widths is characterized, below.

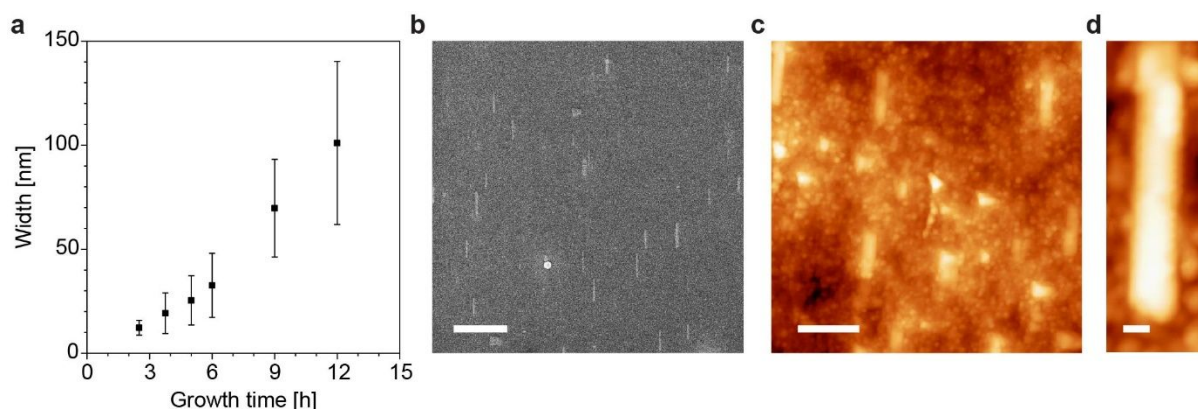


Fig. 4. Growth of narrow nanoribbons on Ge(001)- 9° . (a) Plot of ribbon width *versus* growth time. (b) SEM image of ribbons with average width of 12.2 ± 3.6 nm. (c-d) STM images of nanoribbons with average width of 3–4 nm [$I = 20$ pA, $V = -2$ V (c); $I = 200$ pA, $V = -2$ V (d)]. Scale bars in b-d are 400, 20, and 2 nm, respectively.

2.5. Density functional theory (DFT) calculations

The trapezoidal (Fig. 2e,h) and hemispherical (Fig. 2f,i) islands formed at high growth rates on Ge(001)- 6° and Ge(001)- 9° are similar to crystal shapes observed for graphene growth on Ru(0001)³⁹ and WSe₂ growth on c-plane sapphire.⁴⁰ In the latter cases, the crystal shape is caused by pinning of the uphill edge to a substrate step edge, resulting in a smooth, planar interface that does not grow or grows relatively slowly. In contrast, the downhill edge does not interact as strongly with the substrate, causing it to grow faster in a carpet-like fashion, resulting in a rougher semicircular growth front.

To determine if a similar mechanism is responsible for the crystal shape evolution observed in Fig. 2, we study the stability and edge passivation of ribbons on Ge(001)- 9° using periodic DFT (see Supplementary Information for details). We model armchair nanoribbons ~ 1.5 nm wide on the lowest-energy Ge(001)- 9° surface containing dimerized Ge atoms. The surface is bare because the equilibrium H coverage on Ge is low ($\sim 1/16^{\text{th}}$ monolayer) at typical temperatures and H₂ partial pressures (P_{H_2}) used for growth (Fig. S10). Simulations are performed in which the Ge lattice constant is (1) the calculated relaxed bulk value of 5.67 Å, similar to the experimental value of 5.66 Å, and (2) expanded to 6.04 Å to match the periodicity of the armchair direction and eliminate strain along the ribbon length. It is likely that the Ge lattice constant during graphene growth is between the relaxed and strained values. Nonetheless, at both extremes, the trends observed in our calculations are qualitatively similar.

First, we calculate the minimum-energy structure for ribbons perpendicular to the miscut in which (1) both edges are terminated with H, (2) neither edge is terminated with H, (3) the downhill (uphill) edge is (is not) terminated with H (Fig. 5a,b), and (4) the uphill (downhill) edge is (is not) terminated with H (Fig. 5c,d). When the edges are not terminated with H, the atomic orbitals of C at the ribbon edge and of Ge on the surface rehybridize to form relatively strong covalent bonds, which correspond to regions of large charge transfer as shown in the charge density difference maps in Fig. 5a-d. We accordingly refer to ribbon edges as “pinned” or “unpinned” if they are covalently bonded to Ge or H, respectively.

To determine the thermodynamically-stable edge termination, we construct a phase diagram for ribbons on Ge(001)- 9° exposed to CH₄ and H₂ using the minimum-energy structure for each termination (Fig. 5e). Under typical growth conditions, ribbons with their downhill (uphill) edge pinned (unpinned) are predicted to be the most stable phase by 0.16 and 0.18 eV per edge C atom on relaxed and strained Ge surfaces, respectively (Fig. S11 and S12). The increased stability of the downhill edge is due to energy contributions from the minimum-energy structure of the ribbon, minimum-energy structure of the Ge slab, van der Waals forces, and covalent forces, as summarized in Table 1. More specifically, this increased stability is primarily derived from interactions between the ribbon and the Ge surface, as $\sim 78\%$ and 72% of the total energy difference on relaxed and strained Ge, respectively, are due to van der Waals and covalent forces.

While these calculations provide valuable insight, the phase diagrams only consider ribbons with each edge fully pinned or fully unpinned. Consequently, additional stable ribbon phases with partial Ge- and H-passivated edges may also exist. Nonetheless, these data indicate a larger percentage of C atoms at the downhill edge are pinned than at the uphill edge, and thus the edge termination and

binding strength at the downhill and uphill edges are not equivalent. Moreover, we observe in experiments that Ge below graphene is nanofaceted^{41, 42} (Fig. S13), which is not accounted for in these simulations due to prohibitively large unit cells that are required.

Table 1. Contribution to the total relative stability of nanoribbons with their downhill edge pinned compared to ribbons with their uphill edge pinned. A negative entry means the downhill edge pinned is more stable.

Contribution	Relative energy per edge C atom (downhill pinned – uphill pinned) [eV]	
	Relaxed Ge lattice	Strained Ge lattice
Graphene nanoribbon	-0.01	-0.04
Ge slab	-0.03	-0.01
van der Waals interactions	-0.09	-0.05
Covalent interactions	-0.05	-0.07
Total	-0.18	-0.16

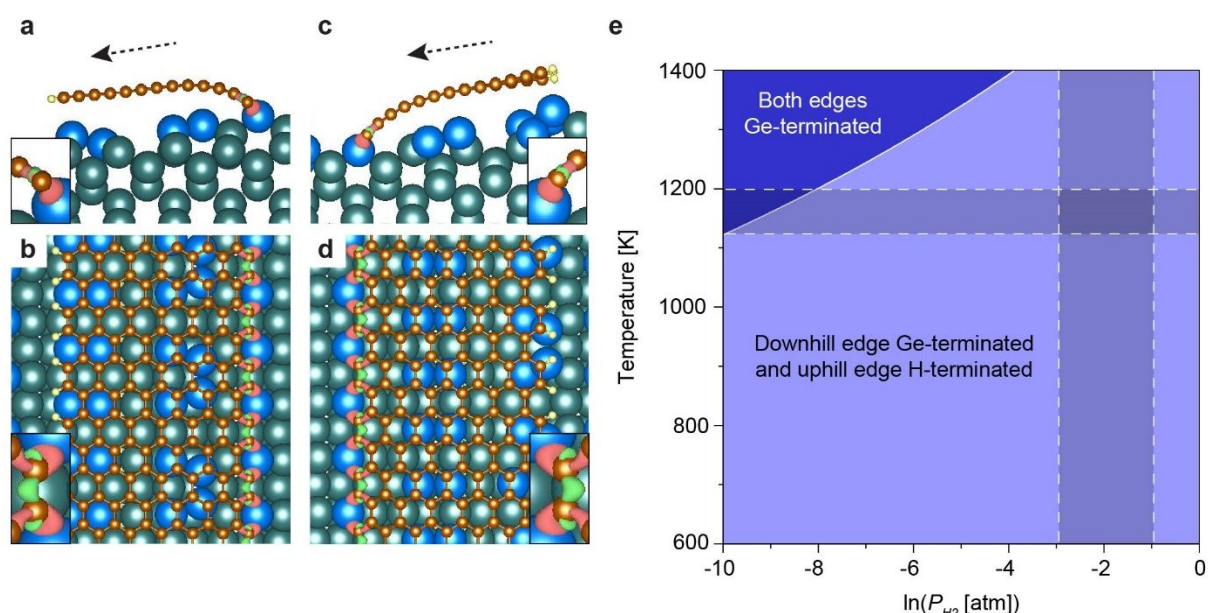


Fig. 5. DFT calculations of graphene nanoribbons on Ge(001)-9°. (a-d) Side (a,c) and top view (b,d) of the minimum-energy structure in which the uphill (downhill) edge is not (is) terminated by H (a,b) and vice versa (c,d). Charge density isosurfaces (insets) show regions of increased (red) and decreased (green) electron density upon ribbon adsorption onto Ge(001)-9°. Green, blue, orange, and white atoms are Ge (saturated, bulk), Ge (unsaturated, surface), C, and H, respectively, and dashed arrows point downhill. (e) Thermodynamic phase diagram plotted against temperature and P_{H_2} . CH_4 partial pressure (P_{CH_4}) is 0.0067 atm. Shaded regions indicate a range of temperatures and P_{H_2} at which ribbons have been synthesized.²⁶ Results in a-e are calculated on strained Ge. Results for relaxed Ge are in Fig. S11 and S12.

2.6. Discussion of anisotropic growth mechanism and formation of smooth armchair edges

It has been shown theoretically⁴³ and experimentally⁴⁴ that on Cu and Ni, graphene growth at slow rates (*i.e.*, low supersaturation) proceeds via a kink-flow mechanism in which growth species add to a smooth crystal edge row-by-row. Growth proceeds via the slow, unfavorable formation of a kink (*i.e.*, the addition of one or more new atoms to an edge), followed by the fast sequential attachment of species to the kink site to propagate the kink along the crystal edge and complete the new atomic row.^{43, 44} The resulting crystals are

terminated with zigzag edges because the zigzag edge is the slowest growing facet on Cu and Ni. If the growth rate is increased (*i.e.*, high supersaturation), attachment is less selective and defects incorporate into the growth front more frequently, resulting in more isotropic growth of crystals with rougher edges.⁴³

On Ge(001)-0°, we have shown armchair facets grow slowest, and growth velocity depends on the angle between the armchair edges and Ge(110).²⁹ We hypothesize that the kink formation rate (and subsequent formation of atomic rows) depends on the graphene edge orientation with respect to the surface. This dependence can be caused by differences in edge termination and

interaction strength of the edge with Ge, which can affect kink formation via factors such as the attachment energy barrier and mechanism, and diffusion of species along the edge, as reported for graphene growth on Cu(111).⁴⁵ We hypothesize the kink formation rate at the short crystal edges is faster than at the long edges. On Ge(001)-0°, we expect this rate at each long edge is the same because the long edges are equivalent. On Ge(001)-6° and Ge(001)-9°, however, we expect the kink formation rate at the long downhill edge is slower than at the long uphill edge because of its increased stability, stronger interaction with Ge, and larger fraction of edge C atoms that are covalently bonded to Ge, as indicated by the DFT calculations above.

We propose when the growth rate is slow, kink formation occurs primarily at the short crystal edges, giving rise to anisotropic growth of ribbons with high-aspect ratios (Fig. 2a,d,g). In particular, on Ge(001)-6° and Ge(001)-9°, the downhill and uphill edges evolve relatively symmetrically as smooth armchair facets because the kink formation rate is relatively slow at both long edges.

In contrast, we propose when the growth rate is fast, the kink formation rate at the uphill edge on Ge(001)-6° and Ge(001)-9° also becomes significant. Consequently, the uphill edge grows faster than the downhill edge and species attach to the uphill edge less selectively (*i.e.*, atomic rows nucleate before the previous row is completed). This rapid, less discriminate growth results in roughening and formation of a more isotropic semicircular growth front, and a decrease in aspect ratio (Fig. 2f,i). Meanwhile, the kink formation rate at the downhill edge also increases but is relatively slow compared to that at the uphill and short edges, resulting in a smooth, straight growth front that evolves row-by-row. With increasing growth rate on Ge(001)-0°, we expect the kink formation rate at the equivalent long edges also increases relative to that at the short edges, resulting in a decrease in aspect ratio (Fig. 2c). However, species still likely add to the long edges more selectively via row-by-row kink flow, as the growth front is fairly straight and does not roughen to the extent of becoming semicircular.

This balance between slow, row-by-row kink-flow growth and fast, less selective, more isotropic growth may explain our observation of increased growth anisotropy and smoother ribbon edges on all Ge(001)-like surfaces in a regime of low supersaturation (*i.e.*, low CH₄ flux or high H₂ flux). Therefore, these results highlight the importance of conducting synthesis in a regime in which growth is particularly slow and may indicate that a strong interaction between the graphene edge and the Ge surface is critical for achieving anisotropic ribbon growth and smooth armchair edges.

2.7. Charge transport properties of narrow graphene nanoribbons

Finally, we conduct room-temperature charge transport measurements of individual narrow ribbons grown on Ge(001)-9° via CVD. Charge transport measurements are conducted using an FET architecture, in which individual nanoribbons are contacted by Cr/Pd/Au source and drain electrodes with channel lengths (L_{ch}) of 30–50 nm, and Si and SiO₂ (15 nm) serve as the gate electrode and gate dielectric, respectively (Fig. 6a). Nanoribbons are synthesized

using high H₂:CH₄ of 50:1 (slow rate of ~30 nm h⁻¹) and short growth time of 2 h (similar to Fig. 4b) to obtain a polydisperse mixture of ribbons with, on average, narrow widths of ~10 nm (standard deviation is roughly 40% of the average width) and aspect ratios > 6.5. Width polydispersity can lead to variability in FET on/off conductance ratio. Nonetheless, the goal of the charge transport measurements is to demonstrate that the ribbons can have high on-state conductance and, in some cases (*i.e.*, when ribbons are particularly narrow), can also exhibit high on/off conductance ratio.

Fig. 6b,c plots source-drain current (I_{ds}) versus source-gate voltage (V_{gs}) on a linear and log scale, respectively, using a source-drain voltage (V_{ds}) of 0.1 V. Hysteresis is exhibited, as expected for ribbons on SiO₂ measured in air.^{46, 47} Moreover, noise is relatively high, as expected for single-ribbon devices, likely due to interactions of ribbons with species originating from the ambient environment. The black, red, and blue curves are measured from three representative ribbons with on/off conductance ratio (G_{on}/G_{off}) of 19, 110, and 570, respectively, and on-state conductance (G_{on}) of 18, 11, and 8.0 μ S, respectively. The high G_{on}/G_{off} of 570 indicates a bandgap $\gg k_B T$ at room temperature is achieved, and the ribbons can be semiconducting rather than semimetallic. G_{on}/G_{off} can vary by orders of magnitude from ribbon to ribbon, which can be attributed to nanoribbon width polydispersity.²⁸ We have recently shown that polydispersity can be reduced by initiating nanoribbon growth on Ge(001)-0° from nanoscale seeds.²⁹ Therefore, polydispersity and the resulting device variability are not necessarily intrinsic limitations of nanoribbon synthesis on Ge via CVD. In future studies, it may be possible to adapt seeded ribbon synthesis on vicinal Ge(001) surfaces to synthesize aligned ribbons with reduced polydispersity. The nanoribbon width in FETs cannot be precisely determined via SEM due to charging from the SiO₂ substrate and screening from the electrodes. However, the ribbon width and bandgap can be estimated from its G_{on}/G_{off} , as shown previously.^{28, 48} From these relationships, a ribbon with G_{on}/G_{off} of 570 has an expected width of ~8 nm and bandgap of ~0.2 eV. Fig. 6d plots I_{ds} against V_{ds} for the ribbon in Fig. 6b,c (blue curve) with G_{on}/G_{off} of 570 and G_{on} of 8.0 μ S at varying V_{gs} . The I_{ds} versus V_{ds} curves are nonlinear at low V_{ds} , indicating G_{on} is likely at least partially limited by a Schottky barrier at the nanoribbon/contact interface.⁴⁹

We plot G_{on} against G_{on}/G_{off} for 18 nanoribbons grown on Ge(001)-9° with $G_{on}/G_{off} > 20$ in Fig. 6e (red stars). Also plotted are data for nanoribbons synthesized via CVD on Ge(001)-0° (black and grey circles)^{26, 28} as well as fabricated using subtractive top-down lithography (blue diamonds),⁵⁰⁻⁵³ narrowing of wider ribbons via etching (green upward triangles),⁵⁴⁻⁵⁶ polymerization/cyclodehydrogenation (orange rightward triangles),¹⁷ sonochemical exfoliation (pink squares),^{48, 57, 58} and unzipping nanotubes (purple downward triangles).^{23, 59} For a given G_{on}/G_{off} , nanoribbons grown on Ge(001)-9° via CVD have among the highest G_{on} of ribbons produced using any method. Similar charge transport has been measured for ribbons grown on Ge(001)-0°, indicating that charge transport is not compromised by growing on the miscut Ge(001)-9° surface.

Nanoscale

ARTICLE

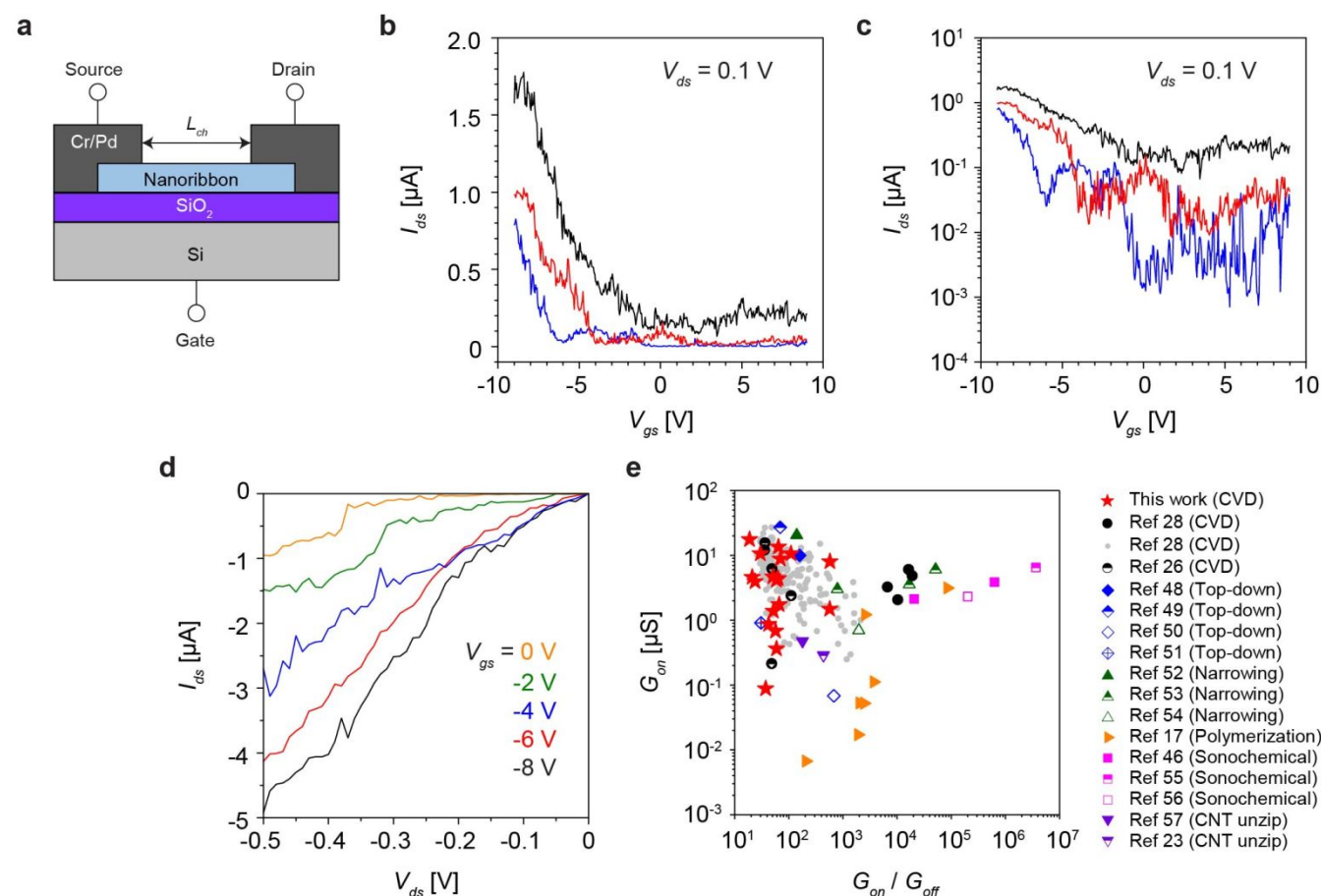


Fig. 6. Charge transport of nanoribbons grown on Ge(001)-9°. (a) FET architecture used for room-temperature transport measurements. (b-c) Plot of I_{ds} versus V_{gs} on a linear (b) and log (c) scale for three nanoribbons at V_{ds} of 0.1 V. Forward sweeps, in which bias is varied from negative to positive voltage, are shown. Reverse sweeps and source-gate current (I_{gs}) versus V_{gs} are plotted in Fig. S14. Hysteresis is exhibited in I_{ds} versus V_{gs} curves, as expected for ribbons on SiO₂ measured in air.^{46,47} (d) Plot of I_{ds} versus V_{ds} for the ribbon in b,c (blue curve) at V_{gs} of 0 to -8 V. (e) Plot of G_{on} versus G_{on}/G_{off} for ribbons grown on Ge(001)-9° via CVD and for ribbons grown via other techniques in the literature.

3. Conclusions

In summary, we show ~90% of the nanoribbons grown on Ge(001)-9° via CVD can be aligned within $\pm 1.5^\circ$ perpendicular to the miscut. The ribbons can have sub-10 nm widths, aspect ratios > 10 on average and as high as 25, and smooth armchair edges – enabled by conducting synthesis using relatively slow growth rate. The nanoribbons display excellent charge transport, simultaneously exhibiting high G_{on} and G_{on}/G_{off} in FETs. The crystal shape evolution with growth rate may indicate a strong interaction between the ribbon edges and the Ge surface is important for achieving

anisotropic growth and ribbons with smooth armchair edges on all Ge(001)-like surfaces. Provided the packing density can be increased (e.g., by seeding growth²⁹ or by increasing nucleation density via growth at lower temperature), large-area alignment of semiconducting nanoribbons on vicinal Ge(001) via CVD could be an important step towards realizing graphene-based semiconductor technologies.

4. Experimental

Graphene synthesis via CVD: Ge(001) substrates with 0° nominal miscut (Wafer World, resistivity > 50 Ω -cm), 6° miscut (University

Wafer, 0.01–0.05 Ω cm, Ga dopants), and 9° miscut (Wafer World, 0.4 Ω cm, Sb dopants) toward Ge[110] are loaded into a horizontal furnace with a quartz tube inner diameter of 34 mm. The system is evacuated to $< 10^{-5}$ torr and then refilled to atmospheric pressure with a flow of Ar and H₂. After annealing the substrates at 910 °C, a flow of CH₄ is introduced to begin graphene synthesis. The furnace is slid away from the growth zone to terminate synthesis while maintaining the atmosphere used during growth. Specific growth conditions used throughout this work are provided in Table S1. We previously found dopants in Ge wafers do not significantly alter growth on Ge(001).²⁶

SEM characterization: After growth, samples are imaged with SEM (Zeiss LEO 1530) using an in-lens detector. Contrast reversal of graphene on Ge (see Fig. 2a–i) is attributed to amorphous carbon deposition upon exposure to the electron beam and oxidation of the Ge surface (Fig. S7 and S8). Amorphous carbon does not affect the measured island size nor shape.

STM characterization: STM images are acquired using a CreaTec STM at 4.5 K with a Nanonis control system and are processed using WSxM.⁶⁰ The system base pressure is 7×10^{-11} mBar. Pt/Ir tips are prepared via electrochemical etching in a CaCl₂ solution and subsequent field emission in-situ. Tip quality and stability is determined by constant height measurements on a clean Au(111) crystal. Samples are annealed overnight at 350 °C and 5×10^{-10} mBar.

AFM characterization: Surface morphology is characterized using atomic force microscopy (AFM) (Veeco MultiMode SPM) in tapping mode.

XRD characterization: The Ge miscut angle and miscut direction are determined with XRD. A low-angle x-ray specular reflection is used to level the sample to within $\pm 0.01^\circ$. The miscut angle is determined by measuring the maximum angle between (004) and the specular direction. The miscut azimuth is determined from the difference between the rotational angle, phi, where the (224) reflection is maximized to the phi where the miscut angle is maximized. Ge(001)-6° and Ge(001)-9° have miscut angles of $5.99 \pm 0.05^\circ$ and $8.75 \pm 0.05^\circ$, respectively, and azimuthal deviation from Ge [110] of $4 \pm 1^\circ$ and $0.5 \pm 1^\circ$, respectively.

LEEM and LEED characterization: The crystallinity of the graphene islands and their registration with Ge(001)-9° are characterized with LEEM and LEED (SPECS Fe-LEEM/PEEM P90). The substrates are annealed at 600 °C for 5 min under ultra-high vacuum (10^{-9} torr) before LEEM and LEED measurements. Incident electron energies of 25–30 eV are used. LEEM and LEED modes are aligned with a precision of $\pm 3^\circ$. To increase contrast of the graphene diffraction spots, samples are tilted relative to the incident electron beam.

TEM and SAED characterization: The TEM and SAED experiments in Fig. 3c,d are conducted in a Tecnai T-12 Cryo TEM at 120 kV. After growth on Ge(001)-9°, the graphene crystals are transferred onto Si₃N₄ windows that are 5 nm in thickness (TEM Windows, product #SN100-A05Q33A), as described previously.²⁹

Raman characterization: Raman spectroscopy in Fig. S3 is conducted using a Thermo-Fisher Scientific DXRxi Raman Imaging Microscope with laser excitation wavelength of 532 nm and power of 10 mW.

DFT calculations: DFT calculations are performed using the PBE-D2^{61, 62} exchange correlation functional as implemented in the

Vienna Ab-Initio Simulation Package (VASP).^{63, 64} k-point sampling is restricted to the Γ point. The Ge substrate is modeled as a slab with eight layers, with the bottom surface passivated by H, the bottom four Ge layers fixed in bulk positions, and the top four Ge layers relaxed. Structures of nanoribbons placed on the Ge surface are optimized, and phase diagrams are constructed by calculating the grand potential of the ribbons exposed to CH₄ and H₂ in the gas phase. A detailed description of the computations is in the Supplementary Information.

Charge transport measurements: Nanoribbons grown on Ge(001)-9° are transferred from Ge onto 15 nm of SiO₂ on Si using a dry transfer method with thermal release tape, as described previously.²⁸ FETs are fabricated using electron-beam lithography to define the source and drain contact regions. Thermal evaporation is used to deposit Cr/Pd/Au (0.7/10/10 nm) contacts. The Si substrate is used as a back gate and 15 nm of SiO₂ is used as the gate dielectric. All devices are measured at room temperature in ambient laboratory conditions using a Keithley 2636A SourceMeter.

Conflicts of interest

There are no conflicts to declare.

Acknowledgements

Research primarily supported by the U.S. Department of Energy, Office of Science, Basic Energy Sciences, under Award No. DE-SC0016007 (R.M.J., C.S., and M.S.A) for graphene growth experiments and characterization of graphene via SEM, TEM, SAED, AFM, and charge transport measurements. Research partially supported by the Robert Draper Technology Innovation Fund (Grant No. 135-AAC6972) and the U.S. Department of Energy, Basic Energy Sciences (DOE-BES), Division of Chemical Sciences (Grant No. DE-FG02-05ER15731) (E.A.M., F.G., and M.M.) for DFT calculations; NSERC Canada (Discovery, SPG, and CRD Grants), Canada Research Chair, Canada Foundation for Innovation, Mitacs, and PRIMA Québec (M.F.-D. and O.M.) and the Natural Science and Engineering Research Council (NSERC) (M.F.-D., P.L.L., O.M., P.D., and R.M.) for characterization of graphene via LEEM and LEED; the National Science Foundation (NSF) under Grant No. 1839199-DMR (W.A.B. and V.B.) and the Wisconsin Alumni Research Foundation (Z.J.K. and V.B.) for STM imaging of nanoribbons; and the U.S. Department of Energy, Office of Science, Basic Energy Sciences, under Award No. DE-FG02-03ER46028 (D.E.S. and M.G.L.) for characterization of Ge via XRD. The authors acknowledge the use of facilities and instrumentation supported by the NSF through the University of Wisconsin Materials Research Science and Engineering Center (Grant No. DMR-1720415).

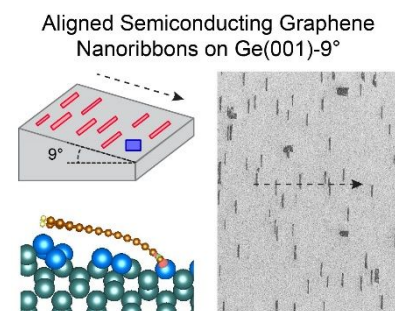
Notes and references

1. L. Yang, C. H. Park, Y. W. Son, M. L. Cohen and S. G. Louie, *Phys. Rev. Lett.* 2007, **99**, 186801.
2. T. Fang, A. Konar, H. Xing and D. Jena, *Phys. Rev. B*, 2008, **78**, 205403.
3. G. C. Liang, N. Neophytou, D. E. Nikonov and M. S.

- Lundstrom, *IEEE Trans. Electron Devices*, 2007, **54**, 677-682.
4. J. Yu, G. X. Liu, A. V. Sumant, V. Goyal and A. A. Balandin, *Nano Lett.*, 2012, **12**, 1603-1608.
 5. M. H. Bae, Z. Y. Li, Z. Aksamija, P. N. Martin, F. Xiong, Z. Y. Ong, I. Knezevic and E. Pop, *Nat. Commun.*, 2013, **4**, 1734.
 6. Q. Zhang, Y. Lu, H. G. Xing, S. J. Koester and S. O. Koswatta, *IEEE Electron Device Lett.*, 2010, **31**, 531-533.
 7. J. Guo, S. Goasguen, M. Lundstrom and S. Datta, *Appl. Phys. Lett.*, 2002, **81**, 1486-1488.
 8. F. Leonard, *Nanotechnology*, 2006, **17**, 2381-2385.
 9. S. Linden, D. Zhong, A. Timmer, N. Aghdassi, J. H. Franke, H. Zhang, X. Feng, K. Mullen, H. Fuchs, L. Chi and H. Zacharias, *Phys. Rev. Lett.*, 2012, **108**, 216801.
 10. P. Ruffieux, J. M. Cai, N. C. Plumb, L. Patthey, D. Prezzi, A. Ferretti, E. Molinari, X. L. Feng, K. Mullen, C. A. Pignedoli and R. Fasel, *ACS Nano*, 2012, **6**, 6930-6935.
 11. L. Talirz, H. Sode, T. Dumschlaff, S. Y. Wang, J. R. Sanchez-Valencia, J. Liu, P. Shinde, C. A. Pignedoli, L. B. Liang, V. Meunier, N. C. Plumb, M. Shi, X. L. Feng, A. Narita, K. Mullen, R. Fasel and P. Ruffieux, *ACS Nano*, 2017, **11**, 1380-1388.
 12. B. V. Senkovskiy, M. Pfeiffer, S. K. Alavi, A. Bliesener, J. Zhu, S. Michel, A. V. Fedorov, R. German, D. Hertel, D. Haberer, L. Petaccia, F. R. Fischer, K. Meerholz, P. H. M. van Loosdrecht, K. Lindfors and A. Gruneis, *Nano Lett.*, 2017, **17**, 4029-4037.
 13. V. Passi, A. Gahoi, B. V. Senkovskiy, D. Haberer, F. R. Fischer, A. Grüneis and M. C. Lemme, *ACS Appl. Mater. Interfaces*, 2018, **10**, 9900-9903.
 14. R. Denk, M. Hohage, P. Zeppenfeld, J. M. Cai, C. A. Pignedoli, H. Sode, R. Fasel, X. L. Feng, K. Mullen, S. D. Wang, D. Prezzi, A. Ferretti, A. Ruini, E. Molinari and P. Ruffieux, *Nat. Commun.*, 2014, **5**, 4253.
 15. P. B. Bennett, Z. Pedramrazi, A. Madani, Y. C. Chen, D. G. de Oteyza, C. Chen, F. R. Fischer, M. F. Crommie and J. Bokor, *Appl. Phys. Lett.*, 2013, **103**, 253114.
 16. M. Ohtomo, Y. Sekine, H. Hibino and H. Yamamoto, *Appl. Phys. Lett.*, 2018, **112**, 021602.
 17. J. P. Llinas, A. Fairbrother, G. B. Barin, W. Shi, K. Lee, S. Wu, B. Y. Choi, R. Braganza, J. Lear, N. Kau, W. Choi, C. Chen, Z. Pedramrazi, T. Dumschlaff, A. Narita, X. L. Feng, K. Mullen, F. Fischer, A. Zettl, P. Ruffieux, E. Yablonovitch, M. Crommie, R. Fasel and J. Bokor, *Nat. Commun.*, 2017, **8**, 633.
 18. M. Y. Han, B. Ozyilmaz, Y. B. Zhang and P. Kim, *Phys. Rev. Lett.*, 2007, **98**, 206805.
 19. Z. H. Chen, Y. M. Lin, M. J. Rooks and P. Avouris, *Phys. E*, 2007, **40**, 228-232.
 20. M. Sprinkle, M. Ruan, Y. Hu, J. Hankinson, M. Rubio-Roy, B. Zhang, X. Wu, C. Berger and W. A. de Heer, *Nat. Nanotechnol.*, 2010, **5**, 727-731.
 21. T. Kato and R. Hatakeyama, *Nat. Nanotechnol.*, 2012, **7**, 651-656.
 22. P. Solis-Fernandez, K. Yoshida, Y. Ogawa, M. Tsuji and H. Ago, *Adv. Mater.*, 2013, **25**, 6562-6568.
 23. L. Y. Jiao, L. Zhang, L. Ding, J. E. Liu and H. J. Dai, *Nano Res.*, 2010, **3**, 387-394.
 24. Y. Joo, G. J. Brady, M. S. Arnold and P. Gopalan, *Langmuir*, 2014, **30**, 3460-3466.
 25. K. R. Jenkins, J. Chan, R. M. Jacobberger, A. Berson and M. S. Arnold, *Adv. Electron. Mater.*, 2018, **0**, 1800593.
 26. R. M. Jacobberger, B. Kiraly, M. Fortin-Deschenes, P. L. Levesque, K. M. McElhinny, G. J. Brady, R. R. Delgado, S. S. Roy, A. Mannix, M. G. Lagally, P. G. Evans, P. Desjardins, R. Martel, M. C. Hersam, N. P. Guisinger and M. S. Arnold, *Nat. Commun.*, 2015, **6**, 8006.
 27. B. Kiraly, A. J. Mannix, R. M. Jacobberger, B. L. Fisher, M. S. Arnold, M. C. Hersam and N. P. Guisinger, *Appl. Phys. Lett.*, 2016, **108**, 213101.
 28. R. M. Jacobberger and M. S. Arnold, *ACS Nano*, 2017, **11**, 8924-8929.
 29. A. J. Way, R. M. Jacobberger and M. S. Arnold, *Nano Lett.*, 2018, **18**, 898-906.
 30. J. H. Lee, E. K. Lee, W. J. Joo, Y. Jang, B. S. Kim, J. Y. Lim, S. H. Choi, S. J. Ahn, J. R. Ahn, M. H. Park, C. W. Yang, B. L. Choi, S. W. Hwang and D. Whang, *Science*, 2014, **344**, 286-289.
 31. J. Y. Dai, D. X. Wang, M. Zhang, T. C. Niu, A. Li, M. Ye, S. Qiao, G. Q. Ding, X. M. Xie, Y. Q. Wang, P. K. Chu, Q. H. Yuan, Z. F. Di, X. Wang, F. Ding and B. I. Yakobson, *Nano Lett.*, 2016, **16**, 3160-3165.
 32. I. Vlassioux, M. Regmi, P. F. Fulvio, S. Dai, P. Datskos, G. Eres and S. Smirnov, *ACS Nano*, 2011, **5**, 6069-6076.
 33. R. M. Jacobberger and M. S. Arnold, *Chem. Mater.*, 2013, **25**, 871-877.
 34. T. Ma, W. C. Ren, X. Y. Zhang, Z. B. Liu, Y. Gao, L. C. Yin, X. L. Ma, F. Ding and H. M. Cheng, *Proc. Natl. Acad. Sci.*, 2013, **110**, 20386-20391.
 35. L. Tao, J. Lee, H. Chou, M. Holt, R. S. Ruoff and D. Akinwande, *ACS Nano*, 2012, **6**, 2319-2325.
 36. R. M. Jacobberger, P. L. Levesque, F. Xu, M.-Y. Wu, S. Choubak, P. Desjardins, R. Martel and M. S. Arnold, *J. Phys. Chem. C*, 2015, **119**, 11516-11523.
 37. X. S. Li, C. W. Magnuson, A. Venugopal, J. H. An, J. W. Suk, B. Y. Han, M. Borysiak, W. W. Cai, A. Velamakanni, Y. W. Zhu, L. F. Fu, E. M. Vogel, E. Voelkl, L. Colombo and R. S. Ruoff, *Nano Lett.*, 2010, **10**, 4328-4334.
 38. C. Teegenkamp, J. Wollschlager, H. Pfnur, F. Heringdorf and M. Horn-von Hoegen, *Phys. Rev. B*, 2002, **65**, 235316.
 39. P. W. Sutter, J. I. Flege and E. A. Sutter, *Nat. Mater.*, 2008, **7**, 406-411.
 40. L. Chen, B. L. Liu, M. Y. Ge, Y. Q. Ma, A. N. Abbas and C. W. Zhou, *ACS Nano*, 2015, **9**, 8368-8375.
 41. K. M. McElhinny, R. M. Jacobberger, A. J. Zaugg, M. S. Arnold and P. G. Evans, *Surf. Sci.*, 2016, **647**, 90-95.
 42. B. Kiraly, R. M. Jacobberger, A. J. Mannix, G. P. Campbell, M. J. Bedzyk, M. S. Arnold, M. C. Hersam and N. P. Guisinger, *Nano Lett.*, 2015, **15**, 7414-7420.
 43. V. I. Artyukhov, Y. Y. Liu and B. I. Yakobson, *Proc. Natl. Acad. Sci.*, 2012, **109**, 15136-15140.
 44. L. L. Patera, F. Bianchini, C. Africh, C. Dri, G. Soldano, M. M. Mariscal, M. Peressi and G. Comelli, *Science*, 2018, **359**, 1243.
 45. P. Li, Z. Li and J. Yang, *J. Phys. Chem. C*, 2017, **121**, 25949-25955.
 46. X. L. Li, X. R. Wang, L. Zhang, S. W. Lee and H. J. Dai, *Science*, 2008, **319**, 1229-1232.
 47. A. Hazeghi, T. Krishnamohan and H. S. P. Wong, *IEEE Trans. Electron Devices*, 2007, **54**, 439-445.
 48. J. W. Bai, X. F. Duan and Y. Huang, *Nano Lett.*, 2009, **9**, 2083-2087.
 49. L. Liao, J. W. Bai, R. Cheng, Y. C. Lin, S. Jiang, Y. Huang and X. F. Duan, *Nano Lett.*, 2010, **10**, 1917-1921.

50. L. A. Ponomarenko, F. Schedin, M. I. Katsnelson, R. Yang, E. W. Hill, K. S. Novoselov and A. K. Geim, *Science*, 2008, **320**, 356-358.
51. Z. H. Pan, N. Liu, L. Fu and Z. F. Liu, *J. Am. Chem. Soc.*, 2011, **133**, 17578-17581.
52. R. Yang, L. C. Zhang, Y. Wang, Z. W. Shi, D. X. Shi, H. J. Gao, E. G. Wang and G. Y. Zhang, *Adv. Mater.*, 2010, **22**, 4014-4019.
53. X. R. Wang and H. J. Dai, *Nat. Chem.*, 2010, **2**, 661-665.
54. L. M. Xie, L. Y. Jiao and H. J. Dai, *J. Am. Chem. Soc.*, 2010, **132**, 14751-14753.
55. X. R. Wang, Y. J. Ouyang, X. L. Li, H. L. Wang, J. Guo and H. J. Dai, *Phys. Rev. Lett.*, 2008, **100**, 206803.
56. X. R. Wang, X. L. Li, L. Zhang, Y. Yoon, P. K. Weber, H. L. Wang, J. Guo and H. J. Dai, *Science*, 2009, **324**, 768-771.
57. L. Y. Jiao, L. Zhang, X. R. Wang, G. Diankov and H. J. Dai, *Nature*, 2009, **458**, 877-880.
58. J. S. Lee, S. Ryu, K. Yoo, I. S. Choi, W. S. Yun and J. Kim, *J. Phys. Chem. C*, 2007, **111**, 12504-12507.
59. W. Kim, A. Javey, O. Vermesh, O. Wang, Y. M. Li and H. J. Dai, *Nano Lett.*, 2003, **3**, 193-198.
60. I. Horcas, R. Fernández, J. M. Gómez-Rodríguez, J. Colchero, J. Gómez-Herrero and A. M. Baro, *Rev. Sci. Instrum.*, 2007, **78**, 013705.
61. J. P. Perdew, K. Burke and M. Ernzerhof, *Phys. Rev. Lett.*, 1996, **77**, 3865-3868.
62. S. Grimme, *J. Comput. Chem.*, 2006, **27**, 1787-1799.
63. G. Kresse and J. Furthmuller, *Comput. Mater. Sci.*, 1996, **6**, 15-50.
64. G. Kresse and J. Furthmuller, *Phys. Rev. B*, 1996, **54**, 11169-11186.

Graphical abstract



Aligned semiconducting armchair graphene nanoribbons with excellent charge transport properties are synthesized on vicinal Ge(001) substrates via chemical vapor deposition.